Turbulence statistics of homogeneous isotropic supercritical fluid flow

David Martín, Joan Grau, and Lluís Jofre*
Department of Fluid Mechanics, Universitat Politécnica de Catalunya, BarcelonaTech (UPC), Barcelona 08019, Spain

(Received 28 August 2025; accepted 2 January 2026; published 28 January 2026)

At supercritical pressures, intermolecular forces and molecular packing effects strongly influence fluid behavior, leading to thermodynamic and transport properties that differ significantly from those at subcritical pressures. At these conditions, the resulting high-pressure thermodynamic state space can be divided into liquidlike and gaslike regimes, separated by the pseudoboiling region, where thermophysical properties change rapidly. In this regard, the effects of real-fluid properties and pseudoboiling phenomena on turbulence at $\mathrm{Re}_\lambda = 30$ and $\mathrm{Ma}_t = 0.1$ are investigated through direct numerical simulations of isotropic turbulence in five thermodynamic states of CO_2: one liquidlike, one gaslike, and three pseudoboiling conditions. The thermophysical operating conditions result in Prandtl numbers greater than one, leading to the generation of sub-Kolmogorov thermal scales. Turbulence statistics are, thus, assessed through spectra, probability density functions, and higher-order moments. Temperature-related quantities are particularly sensitive to supercritical fluid effects, showing increased intermittency in the temperature variance dissipation rate and reduced production of mean-square temperature gradients, particularly in strong pseudoboiling conditions. Finally, local flow topology is analyzed using joint probability density functions of the velocity gradient invariants, conditioned on regions with intense pseudoboiling activity. These regions are found to suppress strain-dominated structures while enhancing vortical motions.

DOI: 10.1103/zkxz-5kvg

I. INTRODUCTION

Fluids at pressures above their critical point are referred to as being in a supercritical state. Understanding the behavior of such fluids is essential due to their widespread relevance in both natural [1] and engineering systems, including propulsion technologies [2,3] and energy generation processes [4,5]. Under supercritical conditions, intermolecular forces and molecular packing effects become significant, resulting in thermodynamic behavior that deviates substantially from that of low-pressure gases. In this regime, nonideal fluid effects are also important, rendering the ideal-gas equation of state (EoS) inadequate. The thermophysical properties of supercritical fluids vary significantly depending on whether the fluid is in a liquidlike or gaslike state. In the liquidlike regime, the fluid is characterized by high densities ρ, low isothermal compressibilities $\beta_T = (1/\rho)(\partial\rho/\partial P)_T$, and transport properties (dynamic viscosity μ and thermal conductivity κ) that decrease with increasing temperature [6]. Conversely, in the gaslike regime, the fluid exhibits

*Contact author: lluis.jofre@upc.edu

lower densities, higher compressibilities, and transport properties that increase with temperature, similar to a gas. The transition between these regimes, at a given pressure, occurs around the pseudoboiling temperature, typically identified by a peak in the specific isobaric heat capacity c_P. Connecting these pseudoboiling temperatures across various pressures defines the pseudoboiling (or Widom) line, which represents a natural extension of the liquid-vapor coexistence line observed in subcritical fluids [7]. This line marks the region where a continuous, second-order transition between liquidlike and gaslike states occurs.

In addition to the complex thermophysical behavior, supercritical fluid turbulence poses significant challenges due to its inherent multiscale nature. The classical Kolmogorov 1941 (K41) theory [8] provides a foundational framework for describing the energy cascade in turbulent flows, wherein energy is transferred from large, problem-dependent scales to progressively smaller, quasi-universal scales through nonlinear interactions [9]. According to K41, the smallest dynamically relevant velocity scale is the Kolmogorov scale, given by $\eta_u = (\nu^3/\langle\varepsilon\rangle)^{1/4}$, where $\nu = \mu/\rho$ is the kinematic viscosity, and $\langle\varepsilon\rangle$ is the mean rate of energy dissipation per unit of mass. Turbulent motions also generate a multiscale structure in convected scalar fields, such as temperature. When the Prandtl number $\mathrm{Pr} = \mu c_P/\kappa$ exceeds unity (i.e., when momentum diffusivity dominates over thermal diffusivity), temperature fluctuations can persist longer and form thermal structures smaller than the Kolmogorov scale. Batchelor [10] estimated the smallest temperature scale in incompressible turbulence as $\eta_T = \eta_u/\sqrt{\mathrm{Pr}}$. If sufficient scale separation exists ($\eta_u \gg \ell \gg \eta_T$), the temperature spectrum exhibits three distinct regimes: an inertial-convective range at scales larger than η_u; a viscous-convective regime between η_u and η_T, characterized by a turbulent kinetic energy scaling of k^{-1}; and a viscous-diffusive regime at scales smaller than η_T [11,12]. In supercritical fluid flows, however, temperature cannot be treated as a passive scalar as strong coupling between temperature and momentum arises from nonlinear thermodynamics and the pronounced dependence of transport properties on both pressure and temperature [13]. In this regard, whether analogous regimes exist under these conditions remains to be determined. Understanding these fine-scale dynamics remains important to clarify their role in the overall turbulence dynamics and to improve modeling strategies for supercritical fluid flows.

Supercritical fluids have primarily been studied using direct numerical simulation (DNS) approaches in wall-bounded or mixing-layer configurations, where externally imposed temperature differences drive the fluid across the pseudoboiling line [14–18]. These configurations naturally introduce large gradients in thermophysical properties and high density ratios, often on the order of 10 [16], which strongly influence the flow dynamics. However, such DNS studies typically do not resolve the Batchelor scale, partly due to its expected limited impact on low-order statistics. In the present study, thus, Batchelor-resolved DNSs of homogeneous isotropic turbulence (HIT) are conducted to isolate the effects of high-pressure thermodynamics and pseudoboiling behavior on turbulence. Previous studies of incompressible HIT have extensively examined the statistical behavior of pressure [19–23] and temperature, or more generally passive scalars [24]. Under such conditions, pressure plays a crucial role in accelerating and deforming the fluid in a way that prevents its dilatation. Its probability density function (PDF) is near Gaussian for positive fluctuations but develops heavy tails on the negative side, resulting in a strongly skewed distribution. These negative excursions have been linked to intense vortical structures [21,23]. Notably, despite being governed by a Poisson equation with velocity gradients as its source term, the pressure field remains negatively skewed even when the velocity field itself is Gaussian [19,20]. Moreover, studies of passive scalars have focused on the scalar cascade and its similarities with the energy cascade [24]. Scalars tend to reach asymptotic isotropic regimes more slowly than velocity fields [25] and exhibit stronger intermittency [26,27], particularly at high Reynolds and Prandtl numbers. Furthermore, scalar dissipation is often localized in filamentlike structures, with limited spatial correlation to regions of intense kinetic energy dissipation [27]. However, the behavior of pressure and temperature fluctuations in real-fluid turbulence remains less well understood, mainly due to the active role of temperature and its strong coupling with the velocity field.

Furthermore, turbulent kinematics have been extensively analyzed using the invariants of the velocity gradient tensor, following the classification approach introduced by Chong and Perry [28]. The joint probability density function (JPDF) of the second and third invariants of the velocity gradient tensor has been observed to exhibit a characteristic "teardrop" shape across a wide range of flow configurations, including incompressible and compressible HIT [28–30], turbulent jets [31], wall-bounded flows [32], and models such as the restricted Euler equations [33]. The JPDF of the invariants can be used to differentiate strain-dominated regions, associated with stretching and mixing, from rotation-dominated ones, which reorient fluid elements with minimal deformation. In compressible turbulence, Pirozzoli and Grasso [29] observed that focal (rotational) structures occupy nearly two-thirds of the flow volume, largely independent of the Mach number. In addition, enstrophy production tends to be enhanced in compressive regions and suppressed in expansive ones [30]. For real-fluid conditions, Sciacovelli *et al.* [34] studied the topology of dense gases (viz. real fluids described by a complex EoS with an inversion zone characterized by a negative fundamental derivative) and observed a weakening of compressive structures and a corresponding enhancement of expansive ones, in contrast to the behavior seen in ideal-gas turbulence.

In this work, therefore, to study how high-pressure (HP) conditions modify turbulence behavior relative to low-pressure (LP) conditions, DNSs of HIT are conducted at various thermodynamic states $\{P, T\}$ in the supercritical regime, spanning one liquidlike, one gaslike, and three pseudoboiling states at different pressures, as well as two equivalent LP cases. The statistical evolution of the thermodynamic state under conservation laws describing fluid motion, as well as the emergence of sub-Kolmogorov temperature scales, is examined. The effects of density and transport-property variations on small-scale statistics, including skewness, flatness, and intermittency, are analyzed for both HP and LP cases. The impact of high-pressure thermodynamic effects and pseudoboiling phenomena on local flow topology is additionally assessed through conditional JPDFs of the velocity gradient invariants. In this regard, the rest of the paper is organized as follows. Section II presents the mathematical framework for studying supercritical fluid flows, including equations of fluid motion, thermodynamic and transport coefficients models, and the forcing scheme employed to sustain turbulence. Section III describes the computational experiments carried out in this work. Section IV investigates the thermodynamic behavior of isotropic turbulence at supercritical fluid conditions. In Sec. V, the statistics of small-scale quantities are studied. Section VI analyzes the flow topology of the small scales, and the impact of the pseudoboiling effects on them. Finally, concluding remarks are given in Sec. VII.

II. FLOW PHYSICS MODELING

The mathematical modeling utilized for studying homogeneous isotropic turbulence at supercritical fluid conditions in terms of (i) equations of fluid motion, (ii) real-fluid thermodynamics, (iii) high-pressure transport coefficients, (iv) solenoidal linear forcing scheme, and (v) numerical methods is described below.

A. Equations of fluid motion

The motion of supercritical fluids is described by the conservation of mass, momentum, and total energy, which in dimensionless form are written as

$$\frac{\partial \rho^\star}{\partial t^\star} + \frac{\partial (\rho^\star u_i^\star)}{\partial x_i^\star} = 0, \tag{1}$$

$$\frac{\partial (\rho^\star u_i^\star)}{\partial t^\star} + \frac{\partial (\rho^\star u_i^\star u_j^\star)}{\partial x_j^\star} = -\frac{\partial P^\star}{\partial x_i^\star} + \mathrm{Re}_{L_0}^{-1} \frac{\partial \tau_{ij}^\star}{\partial x_j^\star} + f_{\rho u_i}^\star, \tag{2}$$

$$\frac{\partial (\rho^\star E^\star)}{\partial t^\star} + \frac{\partial (\rho^\star u_i^\star E^\star)}{\partial x_i^\star} = -\mathrm{Re}_{L_0}^{-1}\mathrm{Pr}_0^{-1}\mathrm{Ec}_0^{-1} \frac{\partial q_i^\star}{\partial x_i^\star} - \frac{\partial (P^\star u_i^\star)}{\partial x_i^\star} + \mathrm{Re}_{L_0}^{-1} \frac{\partial \tau_{ij}^\star u_i^\star}{\partial x_j^\star} + f_{\rho u_i}^\star u_i^\star + f_{\rho E}^\star, \tag{3}$$

where repeated indices imply summation, and superscript $\star$ denotes normalized quantities. Here, t represents time, x_i position in the ith direction, u_i the ith component of the velocity vector, ρ density, and P pressure. The ijth component of the viscous stress tensor is given by $\tau_{ij} = \mu[\partial u_i/\partial x_j + \partial u_j/\partial x_i - (2/3)\delta_{ij}(\partial u_k/\partial x_k)]$, with μ the dynamic viscosity and δ_{ij} the Kronecker delta. The internal and total energy per unit of mass are given by e and $E = e + (u_i u_i)/2$, respectively. The heat conduction flux in the energy equation is modeled by Fourier's law, $q_i = -\kappa(\partial T/\partial x_i)$, with temperature T and thermal conductivity κ. The terms $f_{\rho u_i}$ and $f_{\rho E}$ denote source terms in the ith direction of momentum and total energy, respectively. The obtention of these dimensionless equations is based on the following set of inertial-based scalings [35,36]

$$x_i^\star = \frac{x_i}{L_0}, \quad u_i^\star = \frac{u_i}{u_0}, \quad \rho^\star = \frac{\rho}{\rho_0}, \quad T^\star = \frac{T}{T_0}, \quad P^\star = \frac{P}{\rho_0 u_0^2}, \quad E^\star = \frac{E}{u_0^2}, \quad \mu^\star = \frac{\mu}{\mu_0}, \quad \kappa^\star = \frac{\kappa}{\kappa_0},$$

with subscript 0 denoting reference quantities. The resulting set of scaled equations includes three dimensionless numbers: (i) Reynolds number based on the integral scale $\mathrm{Re}_{L_0} = \rho_0 u_0 L_0/\mu_0$ characterizing the ratio between inertial and viscous forces; (ii) reference Prandtl number $\mathrm{Pr}_0 = \mu_0 c_{P_0}/\kappa_0$ quantifying the ratio between momentum and thermal diffusivity; and (iii) reference Eckert number $\mathrm{Ec}_0 = u_0^2/(c_{P_0} T_0)$ accounting for the ratio between advective mass transfer and heat dissipation potential. Alternatively, the product of the reference Prandtl and Eckert numbers can be rewritten as the reference Brinkman number, $\mathrm{Br}_0 = \mathrm{Pr}_0 \mathrm{Ec}_0$, which quantifies the heat produced by viscous dissipation relative to molecular heat conduction.

B. Real-fluid thermodynamics

The plausible combinations of thermodynamic state variables P, T, and ρ for monocomponent fluids are determined by an EoS. In this work, the Peng-Robinson EoS [37], which is suitable for high-pressure thermodynamic conditions as provided in the work by Jofre and Urzay [3], is utilized to close the equations of fluid motion above. The EoS can be generally expressed in terms of the compressibility factor $Z = P/(\rho R' T)$, where $R' = 188.92\,\mathrm{J/(kg \cdot K)}$ is the specific gas constant for CO_2. In a general dimensionless form, the EoS becomes

$$P^\star = \frac{3Z\rho^\star T^\star}{\hat{\gamma}_0 \mathrm{Ma}_t^2}, \tag{4}$$

where $\hat{\gamma} \approx Z(c_P/c_V)[(Z + T(\partial Z/\partial T)_\rho)/(Z + T(\partial Z/\partial T)_P)]$ is an approximated real-fluid heat capacity ratio [38] with c_V the specific isochoric heat capacity. The dimensionless turbulent Mach number $\mathrm{Ma}_t = \sqrt{3}u_0/c_0$ appears, where c_0 is the sound speed of the reference thermodynamic state, which represents the ratio of flow velocity fluctuations to the reference speed of sound. In addition to the real-fluid EoS, the formulation must be complemented with the necessary thermodynamic potentials at high pressure, such as internal energy and heat capacities, which are obtained from departure functions [39]. These departure functions are employed to transform from ideal-gas conditions (low pressure, only temperature dependent) to supercritical conditions (pressure and temperature dependent). The ideal-gas parts are calculated by means of the NASA 7-coefficient polynomial [40], while the analytical departure expressions to high pressures are derived from the Peng-Robinson EoS [3,41].

C. High-pressure transport coefficients

The high pressures involved in the analyses conducted in this work prevent the use of simple relations for the calculation of μ and κ. In this regard, standard methods for computing these coefficients for Newtonian fluids are based on the correlation expressions proposed by Chung *et al.* [42,43]. These correlation expressions are mainly function of critical temperature T_c and density ρ_c, molar mass M, acentric factor $\mathcal{W}$, association factor κ_a, dipole moment $\mathcal{M}$, and the NASA

7-coefficient polynomial [40]; further details can be found in dedicated works, like for example Poling *et al.* [6] and Jofre and Urzay [3].

D. Solenoidal linear forcing scheme

To sustain statistically stationary, homogeneous, isotropic turbulence in variable-density flows, the solenoidal forcing method of Watanabe *et al.* [44] is employed. The forcing maintains a prescribed root-mean-square velocity u_0, mean dissipation rate per unit of volume $\rho_0\varepsilon_0$, mean pressure P_0 and mean temperature T_0. The mean dissipation rate per unit of mass is defined in terms of the reference velocity and the integral length scale as $\varepsilon_0 = u_0^3/L_0$. The flow is fully characterized by the reference thermodynamic state $\{P_0, T_0\}$, the integral-scale Reynolds number $\mathrm{Re}_{L_0} = \rho_0 u_0 L_0/\mu_0$, and the turbulent Mach number $\mathrm{Ma}_t = \sqrt{3}u_0/c_0$, where thermophysical properties with subscript 0 are evaluated at the reference state $\{P_0, T_0\}$.

A source term of the form $f_{\rho u_i} = C_s \alpha_k \sqrt{\rho} w_i^{(S)}$ is introduced in the momentum equations, where $w_i = \sqrt{\rho} u_i$ is the modified velocity and $w_i^{(S)}$ its solenoidal part, obtained via the Helmholtz decomposition. The nondimensional parameter α_k regulates the instantaneous root-mean-square velocity and is defined as

$$\alpha_k = \left(\frac{\langle u_i u_i \rangle_V - \langle u_i \rangle_V \langle u_i \rangle_V}{3u_0^2} \right)^{-2}, \tag{5}$$

where $\langle \varphi \rangle_V = V^{-1} \iiint \varphi(x, y, z, t)\, dx\, dy\, dz$ denotes the volume average over domain V, with the explicit time dependence omitted for brevity. Time and volume average is analogously denoted by $\langle \varphi \rangle = t_{ave}^{-1} \int \langle \varphi \rangle_V \, dt$. The coefficient C_s is obtained from the volume-averaged kinetic energy transport equation under the assumption that the mean dissipation rate $\langle \tau_{ij} S_{ij} \rangle$ equals $\rho_0 \varepsilon_0$ in the statistically steady state [44]. A spatially uniform, time-dependent cooling term, $f_{\rho E} = -\langle u_i f_{\rho u_i} \rangle_V$, is added to the total energy equation to maintain a constant volume-averaged total energy. Further implementation details are provided in Martín and Jofre [45].

E. Numerical method

The equations of fluid motion are computationally solved by means of the in-house flow solver RHEA [46,47]. The high-pressure numerical framework, including real-fluid thermodynamics and high-pressure transport coefficients, is employed for the high-pressure cases, and validated in Appendix A. A standard semi-discretization procedure is adopted, in which they are firstly discretized in space and then integrated in time. In particular, spatial operators are treated using second-order central-differencing schemes, and time-advancement is explicitly performed by means of a third-order strong-stability preserving Runge-Kutta approach [48]. The convective terms are expanded according to the Kennedy-Gruber-Pirozzoli splitting [49,50], which has been recently extended to supercritical fluid turbulence in previous works [51–53]. The method preserves kinetic energy by convection, and is locally conservative for mass, momentum, and total energy. This numerical framework provides stable computations without the need of any form of artificial dissipation or stabilization procedures.

III. COMPUTATIONAL EXPERIMENTS

Direct numerical simulations of homogeneous isotropic turbulence at high/low-pressure conditions are performed for a Taylor microscale Reynolds number $\mathrm{Re}_\lambda = 30$ and a turbulent Mach number $\mathrm{Ma}_t = 0.1$, where $\mathrm{Re}_\lambda = \sqrt{15\mathrm{Re}_{L_0}}$. The working fluid is carbon dioxide (CO_2), with critical pressure $P_c = 7.38$ MPa, critical temperature $T_c = 304.13$ K, molar mass $M = 0.04401$ kg/mol, and acentric factor $\mathcal{W} = 0.22394$. Five high-pressure cases are considered, with thermodynamic states and corresponding reference Prandtl number summarized in Table I. The cases span three reference reduced pressures: $P/P_c = 1.5$ (case A), $P/P_c = 2$ (cases B, C, and D), and $P/P_c = 5$

TABLE I. Reference thermodynamic conditions and corresponding reference Prandtl numbers using CO_2.

Case	P_0/P_c	T_0/T_{pb}	T_0/T_c	Pr_0
A	1.5	1.00	1.055	3.50
B	2.0	0.95	1.035	1.94
C	2.0	1.00	1.089	2.18
D	2.0	1.05	1.144	1.85
E	5.0	1.00	1.190	1.13
F	0.013	–	0.980	0.76
G	0.013	–	0.980	0.76

(case E). Figure 1 shows the density, normalized by its critical point value (denoted by subscript c), and the specific isobaric heat capacity, normalized by its atmospheric-pressure boiling-point value $c_{P\mathrm{atm,bp}} = 850.85\ \mathrm{J/(kg \cdot K)}$, as functions of the reduced temperature (T/T_c) at these pressures. The reference temperatures of cases A, C, and E are set to the pseudoboiling temperatures, identified by the peak in c_P at each corresponding pressure. In turn, cases B and D represent liquid- and gaslike conditions, respectively, at $P/P_c = 2$. Two additional low-pressure ideal-gas cases are included: one using Sutherland's law for transport properties (case F), and another assuming constant transport properties (case G). Table II presents the dimensional reference parameters for both HP and LP cases.

Simulations are performed on a triple periodic cubic domain of size L, with $L/L_0 = 5.5$ [44,54], and are solved using a 256^3 computational mesh. This domain, together with the employed mesh, provides a sufficient grid resolution to capture the Kolmogorov and Batchelor scales [10], as well as the density gradient scale [55–57]. Validation of the mesh resolution is detailed both in Appendix B and in Martín and Jofre [45]. The simulations are initialized with a uniform pressure P_0 and temperature T_0. An initial velocity field with root-mean-square velocity u_0 is set following the Passot-Pouquet spectrum [58]. After an initial transient, 100 snapshots are taken from the statistically steady state, spaced every t_0 over a total duration of $100\,t_0$, where $t_0 = L_0/u_0$ is the large-eddy turnover time.

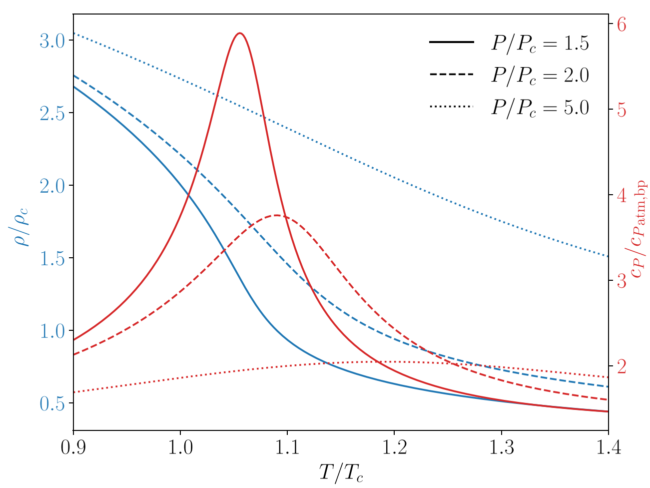

FIG. 1. Normalized density and specific isobaric heat capacity as a function of reduced temperature for the three reduced pressures considered.

TABLE II. Dimensional reference parameters for the HP and LP cases.

Case	P_0 [Pa]	T_0 [K]	ρ_0 [kg/m^3]	u_0 [m/s]	μ_0 [kg/(m s)]	κ_0 [kg m/(s^3 K)]	c_{P_0} [m^2/(s^2 K)]	c_{V_0} [m^2/(s^2 K)]	c_0 [m/s]	L_0 [m]	L [m]
A	11065905.9	320.825	505.747	17.994	3.90×10^{-5}	5.573×10^{-2}	5009.026	686.530	311.667	2.57×10^{-7}	1.41×10^{-6}
B	14754541.2	314.780	726.844	24.190	6.10×10^{-5}	8.766×10^{-2}	2786.441	683.847	418.976	2.08×10^{-7}	1.15×10^{-6}
C	14754541.2	331.347	568.300	20.156	4.44×10^{-5}	6.519×10^{-2}	3197.690	697.432	349.104	2.32×10^{-7}	1.28×10^{-6}
D	14754541.2	347.915	432.309	17.948	3.51×10^{-5}	5.11×10^{-2}	2704.098	710.810	310.865	2.71×10^{-7}	1.49×10^{-6}
E	36886353.0	361.912	770.907	28.689	6.82×10^{-5}	1.054×10^{-1}	1741.925	727.980	496.909	1.85×10^{-7}	1.02×10^{-6}
F	101325.0	298.150	1.799	15.557	1.49×10^{-5}	1.663×10^{-2}	842.622	653.702	269.453	3.20×10^{-5}	1.76×10^{-4}
G	101325.0	298.150	1.799	15.557	1.49×10^{-5}	1.663×10^{-2}	842.622	653.702	269.453	3.20×10^{-5}	1.76×10^{-4}

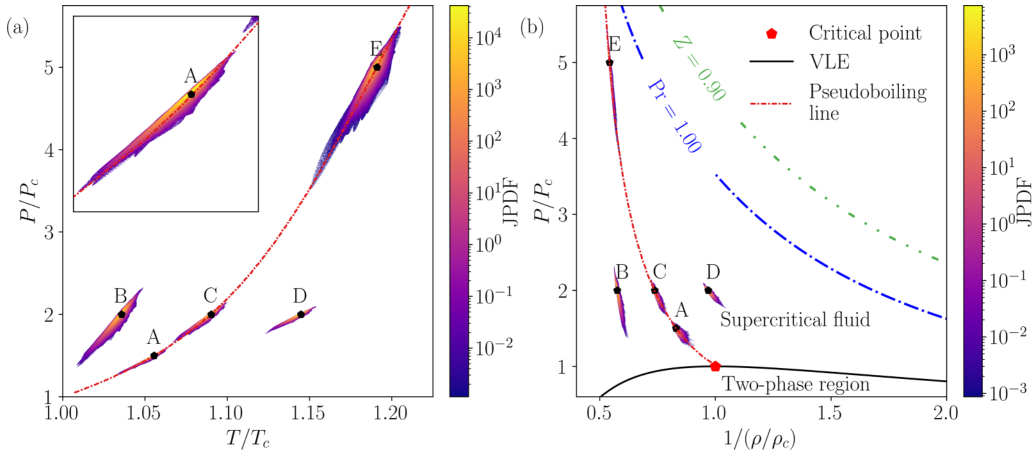

FIG. 2. JPDFs of the thermodynamic state distribution in (a) P-T and (b) P-$1/\rho$ coordinates, normalized by the critical point values, for the five high-pressure simulations.

IV. THERMODYNAMIC BEHAVIOR

The distribution of thermodynamic states, defined by the variables $\{P, T, \rho\}$ and constrained by a HP EoS, under conditions of homogeneous isotropic turbulence is studied in this section. First, the thermodynamic states $\{P, T, \rho\}$ resulting from the natural evolution of the conservation laws are analyzed for the different HP cases in the post-transient regime. Figure 2 presents the JPDFs of the thermodynamic states in normalized (a) P-T and (b) P-$1/\rho$ coordinates for the five HP cases. Under both HP and LP conditions, pressure and temperature exhibit a positive correlation, consistent with their respective EoS (Peng-Robinson and ideal-gas law). The positive correlation between pressure and temperature results in JPDFs in the P-T plane that preferentially align with the pseudoboiling line for the pseudoboiling cases, with fluctuations in the direction perpendicular to the line being especially constrained.

Among the three pseudoboiling cases, those closer to the critical point exhibit a more confined distribution of thermodynamic states in the P-T plane. The limited thermodynamic departures from the reference pseudoboiling state near the critical point are attributed to the elevated c_P in the pseudoboiling region, where a substantial portion of the energy input is consumed by intense molecular rearrangement rather than producing large temperature variations [59]. By contrast, case E displays a broader exploration of thermodynamic states in the P-T plane due to weaker pseudoboiling effects at higher pressures, where c_P is lower and more uniform (see Fig. 1). At a given pressure, the liquid- and gaslike regimes also influence the amplitude of thermodynamic fluctuations under isotropic turbulence. The liquidlike case (case B) exhibits wider variations of pressure and temperature, whereas the gaslike case (case C) shows a more compact distribution. In the P-$1/\rho$ plane, the cases at moderately high pressures exhibit reasonable variations in specific volume ($v = 1/\rho$) despite the low Mach number, driven by the strong density gradients near the critical point. In contrast, the higher-pressure case E exhibits only limited variations along the specific-volume axis, while simultaneously showing stronger departures in the P-T plane under the action of the conservation laws.

The marginal PDFs of normalized pressure and temperature are also examined for both HP and LP cases. Figure 3 presents the marginal PDFs of (a) pressure and (b) temperature fluctuations (denoted by primed variables), normalized by their respective root-mean-square (rms) values, $\sigma_{P'}$ and $\sigma_{T'}$. The pressure distributions are notably skewed, with a strong agreement between LP and HP cases. As observed in incompressible turbulence, positive pressure fluctuations closely follow a Gaussian distribution, whereas negative fluctuations display a pronounced tail [19–23]. The close

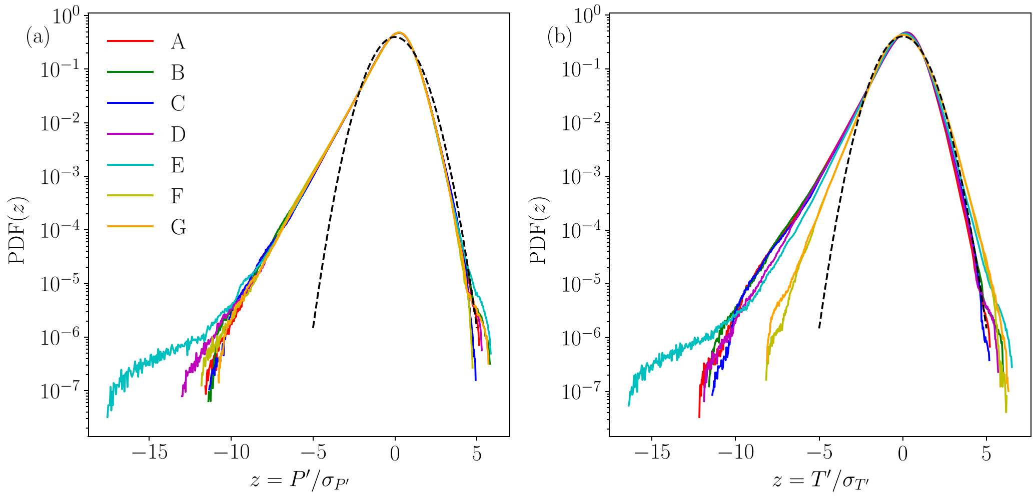

FIG. 3. PDFs of (a) P' and (b) T', normalized by their rms values.

collapse between the HP and LP pressure PDFs with the incompressible behavior is attributed to the low-Mach-number conditions of the simulations. The liquidlike and gaslike cases, which exhibit a wider and narrower spread of pressure fluctuations, respectively, in Fig. 2(a), show an excellent agreement once normalized by their rms values. This suggests that the larger pressure fluctuations observed in the liquidlike regime arise from the higher densities and reference velocities (associated with higher speed of sound), as well as from the inertial pressure scaling $P^\star = P/(\rho_0 u_0^2)$, rather than from a greater degree of intermittency. While case E shows a reasonable agreement with the other cases, large deviations of $P'/\sigma_{P'} \lesssim -10$ are found to be more likely than in the LP and other HP cases. These intense negative pressure fluctuations are rare and may not strongly influence the overall flow behavior, although they can have a disproportionate local impact relative to their frequency. Within the range $-10 \lesssim P'/\sigma_{P'} \lesssim -1$, the PDFs exhibit a stretched exponential behavior of the form

$$\mathrm{PDF}(P'/\sigma_{P'}) \propto \exp[-\beta(P'/\sigma_{P'})^\alpha], \tag{6}$$

where β is a nondimensional Reynolds dependent constant. For both HP and LP cases, the exponent is found to be $\alpha \approx 0.89$.

The temperature fluctuation PDFs exhibit a similar behavior to that of pressure. The distributions show an overall negative skewness, with the positive side roughly following a Gaussian profile and the negative side developing a pronounced heavy tail. In HP cases, the temperature fluctuation distributions more closely resemble those of pressure, exhibiting greater skewness and intermittency than in the LP cases, which in turn display a more symmetric (though still negatively skewed) distribution. Compared to the pressure fluctuation PDFs, the collapse of the heavy tails across HP cases is somewhat weaker, which can be linked to the different Prandtl numbers among HP cases.

The pressure dynamics are further examined through the general pressure transport equation [60], which in dimensionless form is given by

$$\frac{\partial P^\star}{\partial t^\star} = -u_j^\star \frac{\partial P^\star}{\partial x_j^\star} - \rho^\star c_s^{\star 2} \frac{\partial u_j^\star}{\partial x_j^\star} + \frac{\gamma_0}{\mathrm{Re}_{L_0}} \frac{1}{\rho^\star} \frac{\alpha_P^\star}{c_V^\star \beta_T^\star} \left(\mathrm{Ec}_0 \, \tau_{ij}^\star S_{ij}^\star - \frac{1}{\mathrm{Pr}_0} \frac{\partial q_j^\star}{\partial x_j^\star} \right). \tag{7}$$

Figure 4 shows the PDFs of the individual terms contributing to $\partial P^\star/\partial t^\star$ for the HP and LP cases. Both the convective and dilatation terms show a good agreement within the core of the PDFs, with some minor deviations observed in the tails. Among all terms, the normalized viscous dissipation term shows the strongest intermittency, characterized by a heavy positive tail for the different HP

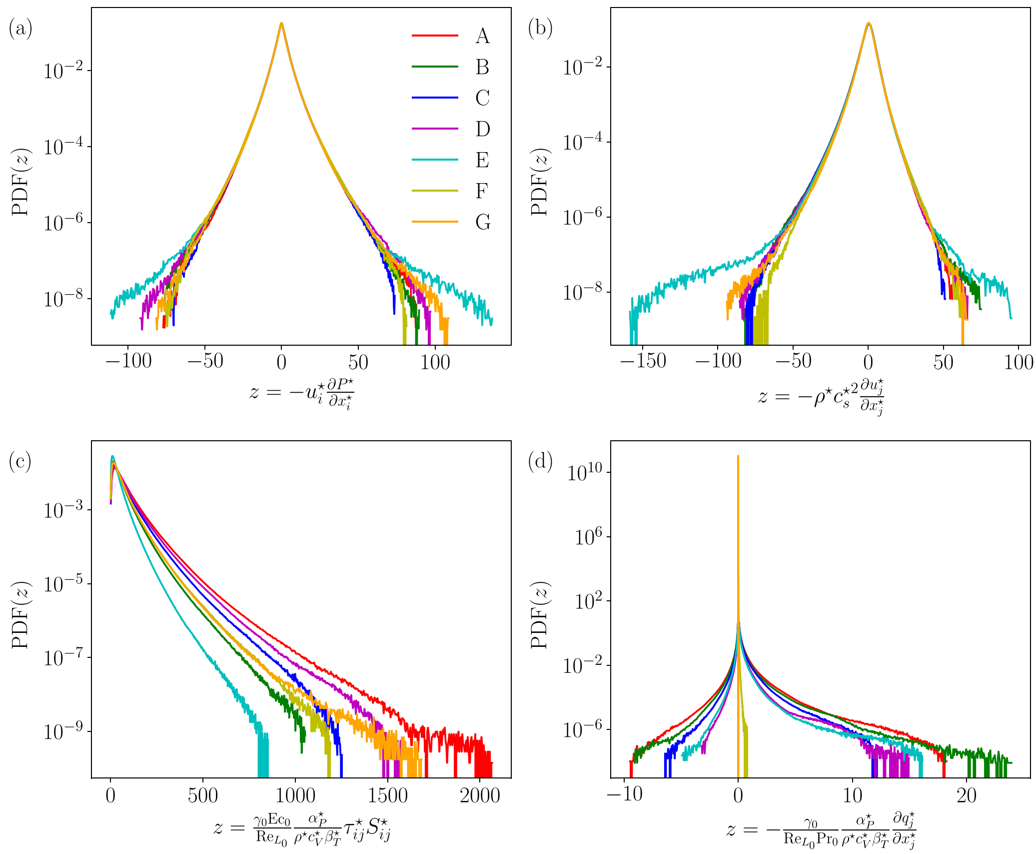

FIG. 4. PDFs of the terms in the pressure transport equation: (a) convective, (b) dilatation, (c) viscous diffusion, and (d) heat flux divergence contributions.

and LP cases. This intermittency is more pronounced in cases where thermodynamic fluctuations are more confined in the thermodynamic planes shown in Fig. 2. While the heat flux contribution is not dominant, it is notably enhanced in HP cases compared to LP ones.

V. SMALL-SCALE PHENOMENOLOGY

The thermodynamic and transport properties of supercritical fluids near the pseudoboiling region, particularly at moderately high pressures, result in Prandtl numbers higher than unity. Under these conditions, smaller-than-Kolmogorov temperature scales are present in the flow. This section, thus, investigates the small-scale behavior of supercritical fluid turbulence using turbulent spectra, PDFs of velocity and temperature gradients, higher-order moments, and statistics of small-scale quantities.

Figure 5 shows the shell-averaged spectra for (a) turbulent kinetic energy and (b) temperature variance across the different cases. Each turbulent kinetic energy and temperature variance spectrum is normalized by $\varepsilon_0^{2/3}\eta_u^{5/3}$ and $\langle\chi\rangle\varepsilon_0^{-1/3}\eta_u^{5/3}$, respectively, where $\chi = 2\kappa(\partial T/\partial x_i)^2/(\rho_0 c_{V_0})$ represents the dissipation rate of temperature variance. The vertical dashed line in each plot marks the wave number associated with the reference Kolmogorov scale η_u. The turbulent kinetic energy spectrum of an incompressible case at a similar Reynolds number ($\mathrm{Re}_\lambda = 36.4$) from the work of Jiménez *et al.* [61] is also included. A good collapse is observed at large scales between the HP, LP, and the reference incompressible cases. Due to the low-Reynolds-number regimes in these simulations, a clear inertial range is not apparent in the turbulent kinetic energy spectra.

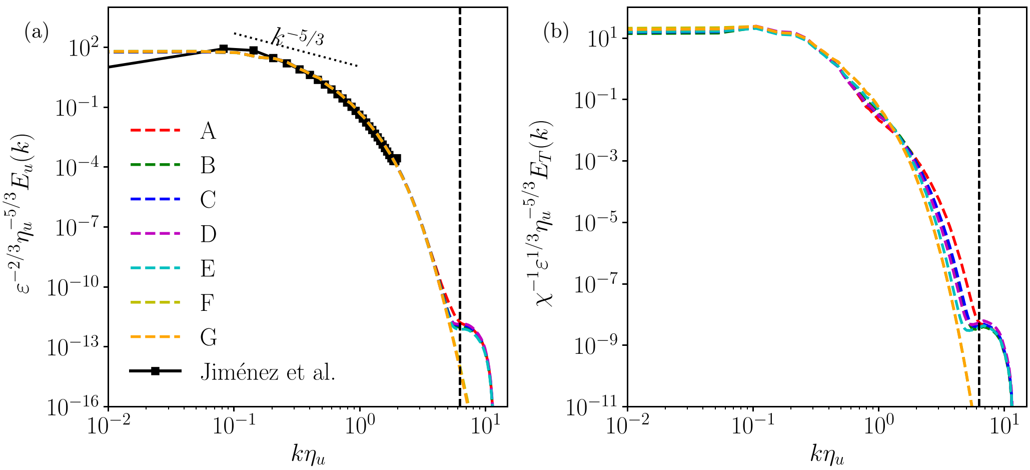

FIG. 5. (a) Turbulent kinetic energy and (b) temperature variance spectra. The vertical line indicates the wave number associated with the Kolmogorov scale, with a normalized value of $k\eta_u = 2\pi$.

The temperature variance spectra shown in Fig. 5(b) follow the same trend at large scales, but HP and LP cases begin to depart at scales slightly larger than the Kolmogorov length. In particular, LP cases exhibit a more rapid energy decay as thermal diffusion becomes more effective at small scales, progressively reducing energy transfer to higher wave numbers. The temperature variance spectra of the HP cases show a similar decay in the inertial-convective regime ($\ell > \eta_u$) but maintain a significantly higher energy content at scales below the Kolmogorov scale, denoted by the vertical dashed line. This behavior, analogous to passive scalar variance spectra in flows with a Prandtl number greater than one [12], reveals the presence of thermal fluctuations at smaller scales in HP cases compared to the LP ones. The Prandtl number effect on the temperature variance spectrum decay is moderate, with higher Pr values (cases closer to the critical point) showing a slightly weaker decay in the inertial-convective regime. Following the increase in small-scale energy content in the temperature spectra, all cases exhibit a rapid decay, with no evidence of a turbulent kinetic energy k^{-1} scaling regime. The absence of a viscous-convective regime analogous to that observed in passive scalars [12] is attributed to the relatively low Prandtl numbers, although such a scaling is not necessarily expected given the active role of temperature in supercritical fluid flows. A higher effective Prandtl number (i.e., thermodynamic states closer to the critical point) would be required to investigate the existence of this regime, at the expense of a significantly higher computational cost for a Batchelor-resolved DNS. In addition, thermodynamic fluctuations around states closer to the liquid-vapor equilibrium curve could potentially drive the system into the vapor-liquid equilibrium (two-phase) region.

A similar increase energetic increase at high wave numbers is also observed in the turbulent kinetic energy spectra [Fig. 5(a)]. This increase originates from small-scale thermophysical fluctuations induced by the strong temperature (and pressure) dependence of fluid properties in high-pressure flows, primarily through density and dynamic viscosity variations. However, the energetic contributions of these scales remains limited: the fraction of velocity variance (kinetic energy) contained at wave numbers larger than the reference Kolmogorov scale,

$$\int_{\eta_u}^{\infty} E_u(k)\,dk \Big/ \int_0^{\infty} E_u(k)\,dk, \tag{8}$$

is significantly smaller than the corresponding contribution of small temperature scales to the total temperature variance,

$$\int_{\eta_u}^{\infty} E_T(k)\,dk \Big/ \int_0^{\infty} E_T(k)\,dk. \tag{9}$$

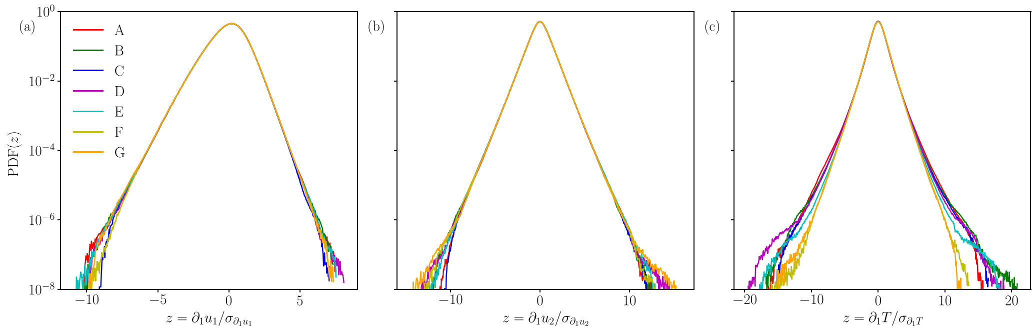

FIG. 6. PDFs of (a) longitudinal velocity gradient, (b) transverse velocity gradient, and (c) temperature gradient, normalized by their rms value, for the different cases.

To investigate the influence of density and transport-property variations on small-scale quantities, the statistical properties of velocity and temperature gradients, including probability density functions and moments, are examined. Figure 6 shows the PDFs of (a) longitudinal velocity gradients ($\partial u_1/\partial x_1$), (b) transverse velocity gradients ($\partial u_2/\partial x_1$), and (c) temperature gradient ($\partial T/\partial x_1$), normalized by their rms value. Despite the higher energetic content observed at high wave numbers in the HP cases, both longitudinal and transverse velocity gradients exhibit similar PDFs in HP and LP cases, with only minor differences appearing in the tails. For all cases, the PDFs of the longitudinal velocity gradients show slight skewness, while the transverse velocity gradients display greater intermittency. Regarding the temperature gradients, the HP cases exhibit consistently broader tails, indicating higher intermittency.

The third and fourth normalized moments, skewness and flatness, are computed for the longitudinal and transverse velocity gradients, as well as for the temperature gradient. These moments are defined as

$$S_\phi = \frac{\langle \phi^3 \rangle}{\langle \phi^2 \rangle^{3/2}} \quad \text{and} \quad F_\phi = \frac{\langle \phi^4 \rangle}{\langle \phi^2 \rangle^2}, \tag{10}$$

where ϕ represents either $\partial_1 u_1 \equiv \partial u_1/\partial x_1$, $\partial_1 u_2 \equiv \partial u_2/\partial x_1$, or $\partial_1 T \equiv \partial T/\partial x_1$. Due to symmetry, the odd moments of the transverse velocity gradient and temperature gradient vanish. In addition, the mixed derivative third- and fourth-order moments [26] are also computed. These are defined as

$$S_{u_1 T} = \frac{\langle (\partial_1 u_1)(\partial_1 T)^2 \rangle}{\langle (\partial_1 u_1)^2 \rangle^{1/2} \langle (\partial_1 T)^2 \rangle} \quad \text{and} \quad F_{u_1 T} = \frac{\langle (\partial_1 u_1)^2 (\partial_1 T)^2 \rangle}{\langle (\partial_1 u_1)^2 \rangle \langle (\partial_1 T)^2 \rangle}. \tag{11}$$

Table III summarizes the computed moments for all cases, together with the standard errors obtained via bootstrap analysis of the snapshots. The skewness of the longitudinal velocity gradient, $S_{\partial_1 u_1}$, remains nearly constant across all cases, with values close to -0.48. This value is known to remain approximately constant up to $\mathrm{Re}_\lambda \approx 80$ in incompressible turbulence studies [26]. Likewise, the flatness of both longitudinal and transverse velocity gradients, $F_{\partial_1 u_1}$ and $F_{\partial_1 u_2}$, shows good agreement among the cases, consistent with the strong similarity observed in their PDFs. Supercritical flows exhibit similar values of $S_{\partial_1 u_1}$, $F_{\partial_1 u_1}$, and $F_{\partial_1 u_2}$ compared with the LP cases, indicating that neither the supercritical state nor the different regions within the supercritical regime affect these quantities, at least for the Reynolds and turbulent Mach numbers considered. The previously observed increase in high-wave-number energy in the turbulent kinetic energy spectra, relative to the LP cases, is found to have no impact on the third- and fourth-order velocity-gradient moments. This is consistent with its small contribution to the total kinetic energy and the dominance of viscous dissipation for $k\eta_u \gtrsim 0.3$ [62]. In contrast, the flatness of the temperature gradient, $F_{\partial_1 T}$, shows pronounced differences between the HP and LP cases. Higher flatness values are observed in the HP cases, indicating a greater occurrence of extreme temperature gradients and, as confirmed later, extreme

TABLE III. Normalized nonzero third- and fourth-order moments of the velocity gradients, temperature gradient, and mixed-gradient moments across the different cases. The corresponding standard error (ES) values, estimated via bootstrap analysis, are also reported.

	Case A	Case B	Case C	Case D	Case E	Case F	Case G
$S_{\partial_1 u_1}$	−0.475	−0.478	−0.478	−0.471	−0.471	−0.473	−0.475
$\mathrm{ES}_{S_{\partial_1 u_1}}$	0.002	0.003	0.002	0.003	0.003	0.002	0.003
$F_{\partial_1 u_1}$	4.020	4.035	4.040	4.038	4.042	4.041	4.056
$\mathrm{ES}_{F_{\partial_1 u_1}}$	0.017	0.015	0.013	0.015	0.017	0.014	0.014
$F_{\partial_1 u_2}$	5.198	5.254	5.237	5.243	5.272	5.258	5.234
$\mathrm{ES}_{F_{\partial_1 u_2}}$	0.021	0.024	0.022	0.025	0.028	0.026	0.025
$F_{\partial_1 T}$	6.731	6.311	6.206	6.270	5.642	5.432	5.399
$\mathrm{ES}_{F_{\partial_1 T}}$	0.136	0.143	0.122	0.129	0.098	0.049	0.045
$S_{u_1 T}$	−0.140	−0.188	−0.165	−0.158	−0.252	−0.333	−0.328
$\mathrm{ES}_{S_{u_1 T}}$	0.002	0.002	0.002	0.002	0.003	0.003	0.003
$F_{u_1 T}$	1.711	1.787	1.745	1.758	1.850	1.888	1.879
$\mathrm{ES}_{F_{u_1 T}}$	0.013	0.013	0.012	0.014	0.013	0.010	0.011

temperature variance dissipation in the HP regime. The flatness in HP cases increases with Prandtl value, suggesting that these extreme events are more frequent in the pseudoboiling region near the critical point. Case E, which does not exhibit strong high-pressure pseudoboiling phenomena, shows a temperature-gradient flatness factor similar to that of the LP cases. This behavior is attributed to its nearly constant c_P and the smoother variations of density and transport properties at higher pressures.

As for the mixed-gradient moments, the third-order moment is negative in all cases, with its magnitude decreasing as the Prandtl number increases. The numerator of this moment, with its sign reversed and without the ensemble-average operator [i.e., $-(\partial u_1/\partial x_1)(\partial T/\partial x_1)^2$], is connected to the production term of mean-square temperature gradient [9,63]. Therefore, HP cases exhibit a reduced production of thermal variance, with the suppression being particularly strong in cases with high pseudoboiling effects. The fourth-order mixed moment, $F_{u_1 T}$, follows a similar trend. HP cases generally show slightly lower values of $F_{u_1 T}$ compared to LP cases, indicating a weaker positive correlation between the squared longitudinal velocity gradient and the squared temperature gradient. Case E, where pseudoboiling effects are significantly weaker, exhibits again mixed moments more comparable to the LP cases. The differences observed in both the temperature-gradient and mixed-gradient moments between the LP and HP cases are found to be meaningful, considering that the Reynolds number is fixed at a relatively low value and that "only" third- and fourth order moments are considered. While higher-order moments would naturally exhibit larger differences, their uncertainty would also increase due to the longer integration times required. In this regard, Table III shows that the observed differences between HP and LP cases exceed the uncertainty of the moments estimated through bootstrap analysis, and are therefore statistically significant. The reported standard errors also provide a measure of the convergence of the moments, particularly for the highest-order (fourth-order) moment considered.

Additionally, the statistics of kinetic energy dissipation rate (ε), enstrophy (Ω), and temperature variance dissipation rate (χ) are examined. The local values of these quantities are defined as $\varepsilon = \tau_{ij} S_{ij}/\langle\rho\rangle$, $\Omega = \omega_i\omega_i$ (with $\omega_i = \varepsilon_{ijk}\partial u_k/\partial x_j$ and ε_{ijk} the Levi-Civita symbol), and $\chi = 2\kappa(\partial T/\partial x_i)^2/(\rho_0 c_{V_0})$. These quantities are closely tied to small-scale structures and are known to exhibit strong intermittency. Extreme values of ε are associated with intense straining, which can trigger, for example, flame extinction [64,65], while high Ω indicates strong vortical motions that can, for instance, enhance particle clustering [66]. At moderate Reynolds numbers, Ω has been shown to be more intermittent than ε [26]; however, at high Reynolds numbers, both tend to scale

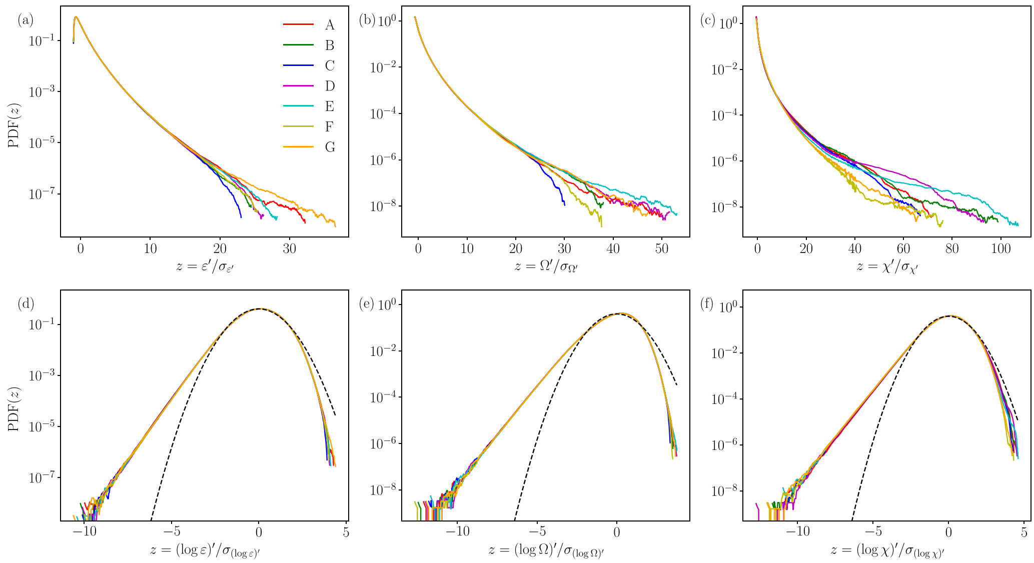

FIG. 7. PDF of (a) turbulent kinetic energy dissipation rate, (b) enstrophy, and (c) temperature variance dissipation rate. (d)–(f) Corresponding PDFs in standardized logarithmic scale.

similarly, and intense events are more likely to occur simultaneously [67]. In contrast, the scalar variance dissipation rates of temperature and mixture fraction are particularly important in turbulent combustion, with accurate modeling of regions with high scalar variance dissipation being essential for reliable large-eddy simulation predictions [68].

Figure 7 presents the PDFs of ε, Ω, and χ for the cases considered. The top row shows the PDFs of the variables, normalized by their mean and standard deviation, while the bottom row shows the PDFs of their logarithms, also standardized. In the linear-scale plots, χ exhibits the highest degree of intermittency, followed by Ω and then ϵ. The velocity-dependent fields (ε and Ω) show excellent collapse across HP and LP cases, with only minor deviations in the likelihood of very intense events, partly due to the inherent limited convergence of these very rare-event statistics. In the PDFs of χ, the HP cases are found to exhibit statistically significantly heavier tails, indicating that extreme temperature variance dissipation events (relative to the standard deviation) are more likely than in LP cases.

In the standardized logarithmic scale, all three quantities deviate from the log-normal distribution originally proposed by Kolmogorov [69] in 1962. Specifically, the log-normal model overestimates the probability of the highest-intensity events for all three variables, while underestimating the probability of extremely small values. However, the PDFs of χ of the HP cases, which were previously identified as the more intermittent, appear closer to log-normal behavior in the right-half of the distribution. The negative tails of the PDFs decay more slowly for $\log \chi$ and $\log \Omega$ than for $\log \varepsilon$, with the tails following a stretched exponential form with estimated decay exponents of $\alpha_{\log \varepsilon} \approx 1.23$, $\alpha_{\log \Omega} \approx 1.16$, and $\alpha_{\log \chi} \approx 1.14$.

The impact of pseudoboiling effects on temperature-related quantities ($\partial_1 T$, χ, and $\log \chi$) is analyzed using conditioned PDFs. Figure 8 presents the unconditioned PDFs of these quantities, along with the PDFs conditioned on regions of pseudoboiling activity, identified by large c_P values, for the intermediate case C. Specifically, the conditioned PDFs are obtained from data surpassing the 75th, 90th, and 95th percentiles of c_P (i.e., the top 25%, 10%, and 5% of the data). Each quantity is normalized using the mean and standard deviation of the unconditioned distribution, and the PDFs are scaled such that the total area under each curve equals one in the normalized coordinates. HP cases not only exhibit heavier tails in the temperature-gradient PFDs, but regions

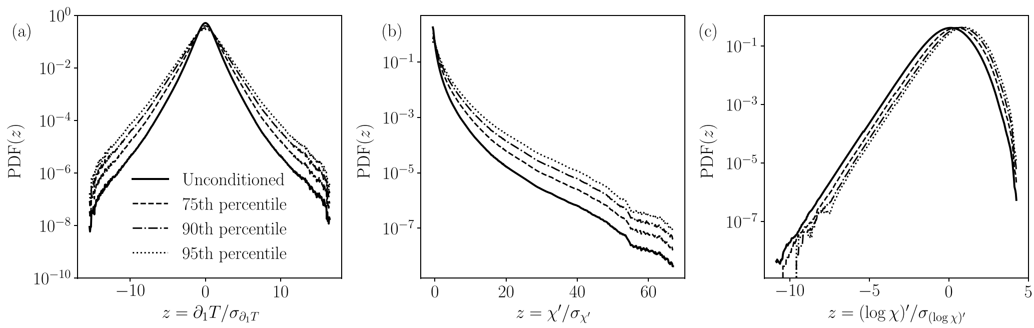

FIG. 8. Conditioned PDFs of (a) temperature gradients, (b) temperature variance dissipation rate, and (c) logarithm of temperature variance dissipation rate for case C, conditioned on regions of high c_P. Solid lines represent the unconditioned PDF, while dashed, dot-dashed, and dotted lines correspond to conditioning on values surpassing the 75th, 90th, and 95th percentile of c_P, respectively.

with strong pseudoboiling activity also contribute disproportionately to the most intense gradients compared with regions of moderate c_P. Similarly, these regions are responsible for a larger fraction of extreme temperature variance dissipation events. The PDFs of logarithm of the temperature variance dissipation rate [Fig. 8(c)] also show that extremely low values of temperature variance dissipation rate become increasingly unlikely as the conditioning increases, indicating an overall enhancement of temperature variance dissipation in regions with high c_P. Conditioned PDFs of the other pseudoboiling cases (cases A and E) show qualitative similar behavior, and are therefore omitted.

VI. SMALL-SCALE FLOW TOPOLOGY

The topology of small-scale structures under HP HIT conditions is examined in this section. To this end, the second-order velocity gradient tensor, with elements $A_{ij} \equiv \partial u_i/\partial x_j$, is considered. The characteristic equation of the velocity gradient tensor is given by $\lambda_i^3 + P\lambda_i^2 + Q\lambda_i + R = 0$, where λ_i are the eigenvalues of the velocity gradient tensor, and P, Q, and R represent the first, second, and third invariants of the tensor, respectively. The invariants are related to the eigenvalues through

$$P = -A_{ii} = -(\lambda_1 + \lambda_2 + \lambda_3), \tag{12}$$

$$Q = \tfrac{1}{2}(P^2 - A_{ij}A_{ji}) = \lambda_1\lambda_2 + \lambda_1\lambda_3 + \lambda_2\lambda_3, \tag{13}$$

$$R = \tfrac{1}{3}(-P^3 + 3PQ - A_{ij}A_{jk}A_{ki}) = -\lambda_1\lambda_2\lambda_3. \tag{14}$$

The velocity gradient tensor can be decomposed into a symmetric rate-of-strain tensor [$\mathrm{S}_{ij} = (A_{ij} + A_{ji})/2$] and a skew-symmetric rate-of-rotation tensor [$\Omega_{ij} = (A_{ij} - A_{ji})/2$]. Their corresponding invariants can be defined analogously and are denoted with subscripts S and Ω, respectively. In particular, $P = P_S$ by definition, and $P_\Omega = R_\Omega = 0$ due to the skew-symmetry of the rate-of-rotation tensor.

The $P{-}Q{-}R$ space can be divided into regions associated with distinct topological behaviors. The discriminant of the velocity gradient tensor, expressed as

$$\Delta = \tfrac{27}{4}R^2 + \left(P^3 - \tfrac{9}{2}PQ\right)R + \left(Q^3 - \tfrac{1}{4}P^2Q^2\right), \tag{15}$$

partitions the space into regions with three distinct real eigenvalues ($\Delta < 0$) and regions with one real and two complex conjugate eigenvalues ($\Delta > 0$). These correspond to strain-dominated (dissipation-prevalent) and rotation-dominated (enstrophy-prevalent) behaviors, respectively [70]. The surface defined by $\Delta = 0$ represents the limit where all eigenvalues are real and two are equal.

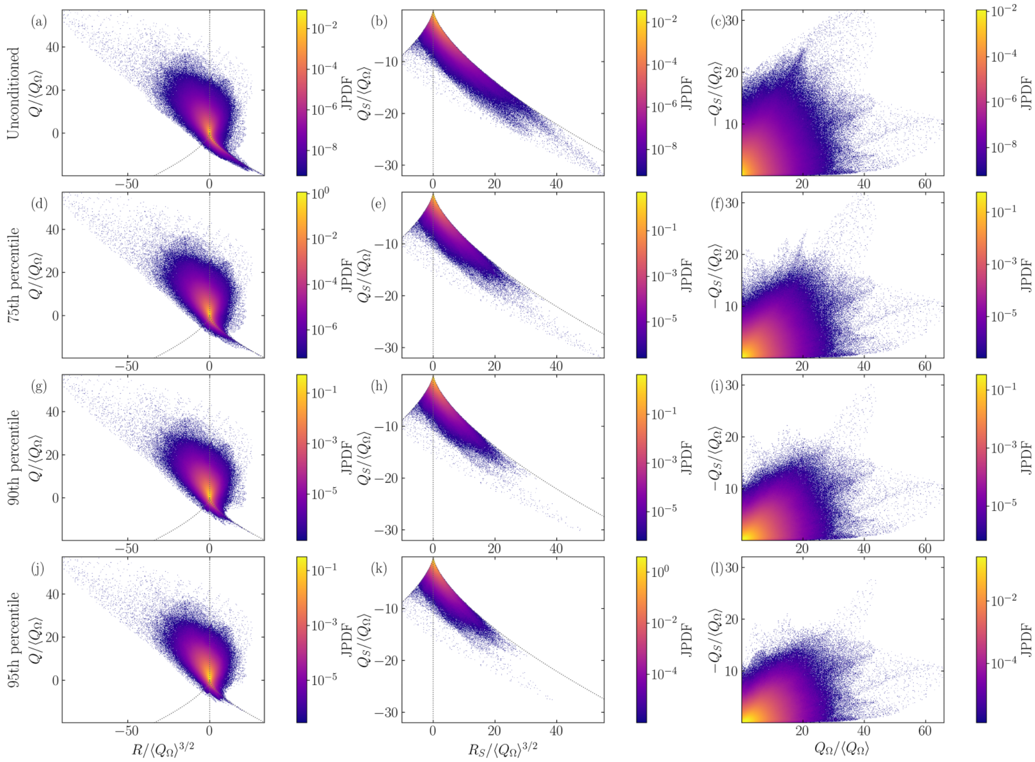

FIG. 9. JPDFs of invariant pairs across three planes for case A. Unconditioned distributions are shown in the (a) (R, Q), (b) (R_S, Q_S), and (c) $(Q_\Omega, -Q_S)$ planes. The second, third, and fourth rows show the same JPDFs as in the first row, but conditioned on the scalar c_P, using only the top 25%, 10%, and 5% of points with the highest c_P values, respectively.

Due to the low-Mach-number conditions of the cases considered, the first invariant results in $P \approx 0$, and the analysis is consequently confined to the Q-R plane. When $P = 0$, further classification of the local flow topology can be made based on the sign of R. For $\Delta > 0$, the topology corresponds to a stable focus/stretching (SF/S) configurations when $R < 0$, and to an unstable focus/compressing (UF/C) configuration when $R > 0$. Conversely, when $\Delta < 0$, a stable node/saddle/saddle (SN/S/S) structure arises for $R < 0$, while an unstable node/saddle/saddle (UN/S/S) topology is associated with $R > 0$.

The JPDFs of (R, Q), (R_S, Q_S), and $(Q_\Omega, -Q_S)$ are shown in panels (a)–(c) of Figs. 9 and 10 for cases A and E, respectively. All invariants are normalized using the mean of the second invariant of the rate-of-rotation tensor $\langle Q_\Omega \rangle$. In the normalized (R, Q) coordinates, the JPDFs exhibit the characteristic teardrop shape found in incompressible turbulence. In line with the findings of Sciacovelli *et al.* [34] for dense gases, the use of complex thermodynamic and transport coefficient models does not appear to significantly alter the kinematic structure of critical points. However, the JPDF distribution is slightly affected, with differences observed between the LP and HP cases, as well as among the HP cases themselves.

Therefore, to examine pseudoboiling effects on the local flow topology, the invariants conditioned on regions of high c_P are also shown in Figs. 9 and 10. Specifically, the second, third, and fourth rows correspond to the same invariants as the first row but computed using only the highest 25%, 10%, and 5% of points based on c_P. Table IV presents the mass fraction corresponding to each topological region previously described, as well as the overall percentages of focal (rotation-dominated) and nonfocal (strain-dominated) regions for the three pseudoboiling cases. In case A,

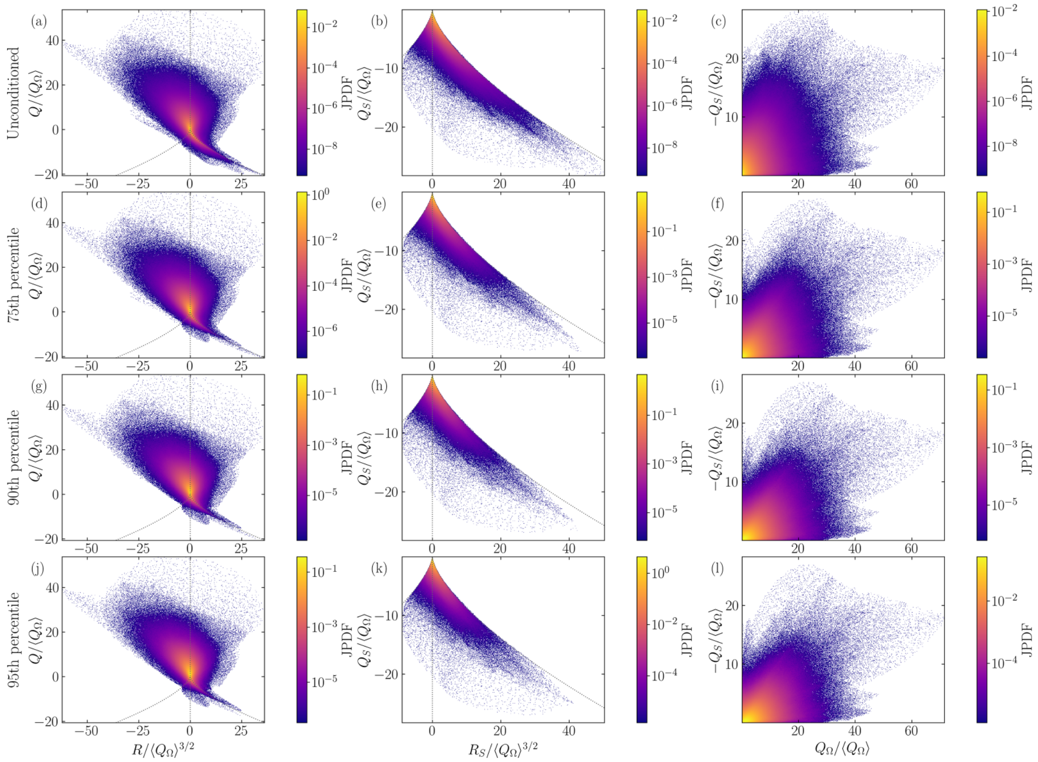

FIG. 10. Unconditioned and conditioned JPDFs of the velocity gradient invariants for case E. Rows and columns follow the same structure as in Fig. 9, with columns corresponding to different invariant planes. The top row shows the unconditioned distributions, while the subsequent rows present the JPDFs conditioned on the scalar c_P, using the top 25%, 10%, and 5% of points with the highest c_P values.

TABLE IV. Percentage of PDF mass in each topological region and in the focal and nonfocal zones, where $Q_{\Delta=0} = -\frac{1}{3}[(27/2)|R|]^{2/3}$.

Case	Percentile	UF/C $R > 0$, $Q > Q_{\Delta=0}$	UN/S/S $R > 0$, $Q \leqslant Q_{\Delta=0}$	SF/S $R < 0$, $Q > Q_{\Delta=0}$	SN/S/S $R < 0$, $Q \leqslant Q_{\Delta=0}$	Focal $Q > Q_{\Delta=0}$	Nonfocal $Q \leqslant Q_{\Delta=0}$
A	Unconditioned	19.86%	13.96%	50.25%	15.94%	70.11%	29.90%
	75	26.95%	3.95%	62.15%	6.94%	89.10%	10.89%
	90	32.20%	2.14%	62.25%	3.41%	94.45%	5.55%
	95	35.19%	1.33%	61.49%	2.00%	96.68%	3.33%
C	Unconditioned	34.97%	22.63%	39.08%	3.32%	74.05%	25.95%
	75	40.19%	7.17%	50.86%	1.78%	91.05%	8.95%
	90	41.46%	3.67%	53.80%	1.07%	95.26%	4.74%
	95	42.38%	2.13%	54.79%	0.70%	97.17%	2.83%
E	Unconditioned	38.64%	31.09%	28.90%	1.37%	67.54%	32.46%
	75	45.61%	11.26%	42.30%	0.84%	87.91%	12.10%
	90	46.14%	5.93%	47.36%	0.57%	93.50%	6.50%
	95	46.45%	3.36%	49.81%	0.38%	96.26%	3.74%

the flow topology states are preferentially concentrated in the SF/S region, which accounts for approximately 50% of the data, while the remaining data is roughly evenly distributed among the three other topologies. As the conditioning on c_P becomes more restrictive, the presence in the UN/S/S and SN/S/S regions diminishes, while the proportion of UF/C and SF/S regions increases. This trend is clearly visible in Figs. 9(a), 9(d), 9(g), and 9(j), where the tail of the teardrop gradually disappears with stronger conditioning. Moreover, conditioning the JPDFs on regions of high c_P reveals an overall enhancement of focal structures, with their volume fraction increasing from approximately 70% to 97%, as reflected in the last two columns of Table IV. In contrast, case E is predominantly found in a UF/C state, followed closely by UN/S/S and SF/S regions. Conditioning the data once again enhances the prevalence of focal structures; however, in this case, the distribution between UF/C and SF/S becomes more balanced. Despite exhibiting a similar focal to nonfocal proportion as case A, the characteristic tail of the teardrop shape persists, due to a comparatively higher percentage of states in the UN/S/S region.

Conditioning effects are also evident in the (R_S, Q_S) plane. Due to the symmetry of the rate-of-strain tensor, all eigenvalues are real, and the JPDF is confined to the region where $\Delta = (27/4)R_S^2 + Q_S^3 \leqslant 0$. In the unconditioned plots of Figs. 9 and 10, a clear bias is observed toward the right-hand branch of the curve $Q_{\Delta=0} = -\frac{1}{3}[(27/2)|R|]^{2/3}$, corresponding to biaxial extension/axisymmetric expansion [70,71], characterized by the eigenvalue ratio $1:1:-2$. Applying the c_P-based conditioning significantly suppresses the occurrence of strong biaxial extension events. In contrast, the region associated with uniaxial extension/axisymmetric contraction, represented by states along the left-hand branch defined by $Q_{\Delta=0}$ for negative R, remains largely unaffected. With stronger conditioning, the concentration of the probability mass shifts toward the origin, indicating suppression of strong strain states. The constraining effect is notably weaker in case E, where pseudoboiling effects are less pronounced and characterized by a more uniform c_P field and milder gradients in ρ, μ, and κ.

Finally, in the $(Q_\Omega, -Q_S)$ plane, the impact of conditioning is more subtle. Instances of large-magnitude Q_S combined with low Q_Ω, where energy dissipation rate dominates [71], become increasingly rare as the conditioning becomes stricter, accompanied by a strengthening of enstrophy-dominated motions. However, consistent with earlier observations, this effect weakens with increasing pressure, reflecting the diminishing influence of pseudoboiling effects.

VII. SUMMARY AND CONCLUSIONS

Direct numerical simulations of homogeneous isotropic turbulence under supercritical fluid conditions have been conducted for five thermodynamic states of CO_2: a gaslike, a liquidlike, and three pseudoboiling states at different pressures, at $\mathrm{Re}_\lambda = 30$ and $\mathrm{Ma}_t = 0.1$. The influence of high-pressure thermophysical properties and pseudoboiling phenomena on turbulence statistics has been examined and compared against two equivalent low-pressure reference cases.

The analysis of thermodynamic behavior of supercritical HIT indicates that natural thermodynamic fluctuations in the pseudoboiling cases tend to align with the pseudoboiling line in the P-T plane. At moderate pressures, where pseudoboiling effects are more pronounced, fluctuations in the P-T directions are strongly suppressed, favoring variability along the specific volume axis. As pressure increases, larger fluctuations are observed in the P-T plane, accompanied by a corresponding reduction in specific-volume variability. Larger deviations in thermodynamic variables from the reference state are observed in the liquidlike regime, primarily due to the thermodynamic properties in the liquidlike region, specifically density and speed of sound, together with the inertial scaling of pressure. Despite the higher fluctuations, pressure intermittency remains largely unaffected between low-pressure and the various high-pressure thermodynamic regimes, aside from minor deviations in the distribution of tails at the highest pressure. In contrast, temperature distributions under high-pressure conditions exhibit increased skewness and stronger intermittency. This increase in intermittency is primarily driven by the higher coupling between the thermodynamic quantities in supercritical fluids.

Spectral analysis reveals the presence of thermal fluctuations at scales smaller than the Kolmogorov length scale for HP cases. This is attributed to Prandtl values greater than one in the high-pressure cases. Velocity and temperature fields have been examined, showing that density and transport-property variations do not significantly alter velocity fields, whereas more pronounced differences with respect the low-pressure cases are observed for temperature-related quantities. with the latter exhibiting more pronounced differences compared to the low-pressure cases. Specifically, both temperature gradients and the dissipation rate of temperature variance display more extreme events in high-pressure cases, with intermittency increasing with Prandtl number. Additionally, regions with strong pseudoboiling effects contribute more than regions with moderate pseudoboiling effects to intense temperature gradients and extreme temperature dissipation events. The increase in intermittency in high-pressure cases results in a PDF distribution of the logarithm of temperature variance dissipation rate that aligns closer to the right side of a log-normal distribution. Furthermore, mixed moments indicate a reduction in the production of mean-square temperature gradients under high-pressure conditions, particularly in cases exhibiting strong pseudoboiling effects. Finally, the small-scale topology has been examined using JPDFs of the invariants of the velocity gradient tensor. Conditioning on regions of high specific isobaric heat capacity, indicative of strong pseudoboiling effects, reveals an enhancement of vortical structures and a suppression of nonfocal topologies for all the pseudoboiling cases. This findings, observed in CO_2, are expected to extend to other supercritical fluids through the principle of corresponding states [72,73].

This work has focused on several thermodynamic conditions at a fixed $\mathrm{Re}_\lambda = 30$ and turbulent Mach number $\mathrm{Ma}_t = 0.1$. Thus, the effects of higher Reynolds numbers and moderate Mach numbers on turbulence statistics, intermittency, and scaling remain to be explored. In particular, higher Reynolds and Mach numbers are expected to develop a wider range of pressure and temperature fluctuations, with a corresponding increase in thermophysical property variations. The full implications of high-pressure velocity–temperature coupling and supercritical small-scale features on turbulence at higher Reynolds remain open questions for future investigation.

ACKNOWLEDGMENTS

This work is funded by the European Union (ERC, SCRAMBLE, Grant No. 101040379). Views and opinions expressed are however those of the authors only and do not necessarily reflect those of the European Union or the European Research Council. Neither the European Union nor the granting authority can be held responsible for them. The authors gratefully acknowledge support from the *Joan Oró* scholarship (Grant No. 2024 FI-1 00205), the SGR program (Grant No. 2021-SGR-01045) of the Generalitat de Catalunya (Catalonia), and Grant No. PID2023-150840OA-I00 of the Agencia Estatal de Investigación (AEI, Spain).

DATA AVAILABILITY

The data that support the findings of this article are openly available [74].

APPENDIX A: THERMOPHYSICAL PROPERTIES VALIDATION

The high-pressure framework implemented in RHEA [46,47], comprising the Peng-Robinson [37] real-fluid EoS and thermodynamic potentials, as well as the transport coefficients model proposed by Chung *et al.* [42,43], is validated across a range of temperatures at the three working pressures of the HP cases. These models have been widely adopted in recent high-fidelity simulations [2,16,17,75,76], and their ability to accurately capture real-fluid properties in high-pressure flows crossing the pseudoboiling line has been discussed in works such as Hickey *et al.* [77], Congiunti *et al.* [78] and Guo *et al.* [16]. Figure 11 compares the normalized (a) density and (b) dynamic viscosity of CO_2 obtained with the models implemented in RHEA against reference data from the NIST database [79]. The agreement is remarkable, particularly in the vicinity of the

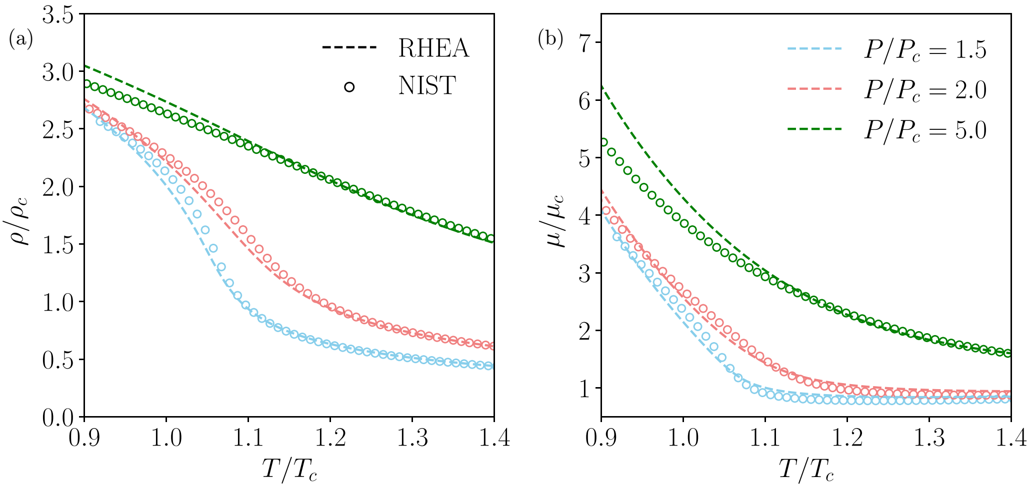

FIG. 11. Comparison between the thermodynamic and transport coefficient model and the NIST database for CO_2 of normalized (a) density and (b) dynamic viscosity for three working pressures.

reference thermodynamic states of the five HP cases. Additional information on the accuracy of the models in the supercritical regime can be found in Martín and Jofre [45].

APPENDIX B: MESH VALIDATION

The standard mesh resolution for HIT in incompressible flows is typically set at $k_{\max}\eta_u = 1.5$, where $k_{\max} = \pi N/L$ is the highest wave number in each direction. In physical space, this corresponds to $\Delta h/\eta_u = \pi/1.5 \approx 2.1$, with Δh denoting the uniform grid spacing. This resolution is sufficient to capture low-order statistics [62], although higher resolutions are required to accurately resolve high-order statistical moments and intermittent high-intensity events [80,81]. For supercritical fluid flows, however, the mesh requirements for HIT need to be reassessed. In particular, the higher-than-unity Prandtl numbers in the vicinity of the pseudoboiling region, together with the enhanced velocity-temperature coupling, result in both smaller velocity and temperature scales than in low-pressure turbulence. In addition, the large density gradients observed across the pseudoboiling line introduce an additional characteristic limiting scale that must be resolved, which can be estimated as $\delta_{\nabla\rho} = (\rho_{\max} - \rho_{\min})/(|\nabla\rho|_{\max})$ [55,56,82].

In this work, thus, all simulations are performed on a 256^3 computational mesh. For the most demanding case (case A, with $\mathrm{Pr}_0 = 3.5$), this corresponds to a resolution with fully populated spherical shells [62] up to $k_{\max}\eta_u \approx 6.78$ and $k_{\max}\eta_T \approx 3.62$, relative to the Kolmogorov ($\eta_u = [(\mu_0/\rho_0)^3/\varepsilon_0]^{1/4}$) and the Batchelor ($\eta_T = \eta_u/\sqrt{\mathrm{Pr}_0}$) scales. In physical space, the grid spacing relative to these scales is $\Delta h/\eta_u \approx 0.46$ and $\Delta h/\eta_T \approx 0.87$, indicating that both are resolved. This resolution is finer than that employed in previous studies of high-pressure transcritical flows [15,16,57], including those specifically targeting small-scale dynamics [17], and comparable to the ones used to capture high-order moments in incompressible turbulence [80,83]. Moreover, the density-gradient scale is estimated to be approximately 3.7 times the Kolmogorov scale, and is therefore also well resolved.

[1] S. Lebonnois and G. Schubert, The deep atmosphere of venus and the possible role of density-driven separation of CO_2 and N_2, Nat. Geosci. **10**, 473 (2017).

[2] J. P. Hickey and M. Ihme, Supercritical mixing and combustion in rocket propulsion, Annual Research Briefs, Center for Turbulence Research, Stanford University 21 (2013), https://web.stanford.edu/group/ctr/ResBriefs/2013/02_hickey.pdf.

[3] L. Jofre and J. Urzay, Transcritical diffuse-interface hydrodynamics of propellants in high-pressure combustors of chemical propulsion systems, Prog. Energy Combust. Sci. **82**, 100877 (2021).

[4] P. C. Ma, L. Bravo, and M. Ihme, Supercritical and transcritical real-fluid mixing in diesel engine applications, Proceedings of the Summer Program 2014, Center for Turbulence Research, Stanford University, 99 (2014).

[5] C. Crua, J. Manin, and L. M. Pickett, On the transcritical mixing of fuels at diesel engine conditions, Fuel **208**, 535 (2017).

[6] B. E. Poling, J. M. Prausnitz, and J. P. O'Connell, *Properties of Gases and Liquids*, 5th ed. (McGraw Hill, New York, NY, 2001)

[7] D. T. Banuti, M. Raju, and M. Ihme, Similarity law for Widom lines and coexistence lines, Phys. Rev. E **95**, 052120 (2017).

[8] A. N. Kolmogorov, The local structure of turbulence in incompressible viscous fluid for very large Reynolds numbers, Proc. R. Soc. London, Ser. A **434**, 9 (1991).

[9] K. R. Sreenivasan and R. A. Antonia, The phenomenology of small-scale turbulence, Annu. Rev. Fluid Mech. **29**, 435 (1997).

[10] G. K. Batchelor, Small-scale variation of convected quantities like temperature in turbulent fluid— Part 1. General discussion and the case of small conductivity, J. Fluid Mech. **5**, 113 (1959).

[11] D. A. Donzis, K. R. Sreenivasan, and P. K. Yeung, The Batchelor spectrum for mixing of passive scalars in isotropic turbulence: Submitted for the special issue dedicated to S. B. Pope, Flow Turbul. Combust. **85**, 549 (2010).

[12] M. Mohaghar, L. P. Dasi, and D. R. Webster, Scalar power spectra and turbulent scalar length scales of high-Schmidt-number passive scalar fields in turbulent boundary layers, Phys. Rev. Fluids **5**, 084606 (2020).

[13] J. Bellan, Future challenges in the modelling and simulations of high-pressure flows, Combust. Sci. Technol. **192**, 1199 (2020).

[14] R. S. Miller, K. G. Kenneth, and J. Bellan, Direct numerical simulations of supercritical fluid mixing layers applied to heptane–nitrogen, J. Fluid Mech. **436**, 1 (2001).

[15] S. Kawai, Heated transcritical and unheated non-transcritical turbulent boundary layers at supercritical pressures, J. Fluid Mech. **865**, 563 (2019).

[16] J. Guo, X. I. A. Yang, and M. Ihme, Structure of the thermal boundary layer in turbulent channel flows at transcritical conditions, J. Fluid Mech. **934**, A45 (2022).

[17] F. Li, W. Zhang, B. Bai, and M. Ihme, Small-scale turbulent characteristics in transcritical wall-bounded flows, J. Fluid Mech. **986**, A36 (2024).

[18] C. Monteiro and L. Jofre, Flow regime analysis of high-pressure transcritical fluids in microducts, Int. J. Heat Mass Transf. **224**, 125295 (2024).

[19] M. Holzer and E. Siggia, Skewed, exponential pressure distributions from Gaussian velocities, Phys. Fluids **5**, 2525 (1993).

[20] A. Pumir, A numerical study of pressure fluctuations in three-dimensional, incompressible, homogeneous, isotropic turbulence, Phys. Fluids **6**, 2071 (1994).

[21] T. Gotoh and R. S. Rogallo, Statistics of pressure and pressure gradient in homogeneous isotropic turbulence, Proceedings of the Summer Program 1994, Center for Turbulence Research, Stanford University (1994).

[22] T. Gotoh and R. S. Rogallo, Intermittency and scaling of pressure at small scales in forced isotropic turbulence, J. Fluid Mech. **396**, 257 (1999).

[23] N. Cao, S. Chen, and G. D. Doolen, Statistics and structures of pressure in isotropic turbulence, Phys. Fluids **11**, 2235 (1999).

[24] Z. Warhaft, Passive scalars in turbulent flows, Annu. Rev. Fluid Mech. **32**, 203 (2000).

[25] K. R. Sreenivasan, On local isotropy of passive scalars in turbulent shear flows, Proc. R. Soc. A: Math. Phys. Eng. Sci. **434**, 165 (1991).

[26] R. M. Kerr, Higher-order derivative correlations and the alignment of small-scale structures in isotropic numerical turbulence, J. Fluid Mech. **153**, 31 (1985).
[27] P. Vedula, P. K. Yeung, and R. O. Fox, Dynamics of scalar dissipation in isotropic turbulence: A numerical and modelling study, J. Fluid Mech. **433**, 29 (2001).
[28] M. S. Chong and A. E. Perry, A general classification of three-dimensional flow fields, Phys. Fluids **2**, 765 (1990).
[29] S. Pirozzoli and F. Grasso, Direct numerical simulations of isotropic compressible turbulence: Influence of compressibility on dynamics and structures, Phys. Fluids **16**, 4386 (2004).
[30] J. Wang, Y. Shi, L.-P. Wang, Z. Xiao, X. T. He, and S. Chen, Effect of compressibility on the small-scale structures in isotropic turbulence, J. Fluid Mech. **713**, 588 (2012).
[31] P. Thaker, J. Mathew, and S. Ghosh, Invariants of the velocity gradient tensor in a spatially developing compressible round jet, J. Fluid Mech. **971**, A18 (2023).
[32] H. M. Blackburn, N. N. Mansour, and B. J. Cantwell, Topology of fine-scale motions in turbulent channel flow, J. Fluid Mech. **310**, 269 (1996).
[33] B. J. Cantwell, Exact solution of a restricted Euler equation for the velocity gradient tensor, Phys. Fluids A **4**, 782 (1992).
[34] L. Sciacovelli, P. Cinnella, and F. Grasso, Small-scale dynamics of dense gas compressible homogeneous isotropic turbulence, J. Fluid Mech. **825**, 515 (2017).
[35] L. Jofre, Z. R. del Rosario, and G. Iaccarino, Data-driven dimensional analysis of heat transfer in irradiated particle-laden turbulent flow, Int. J. Multiphase Flow **125**, 103198 (2020).
[36] L. Jofre, M. Bernades, and F. Capuano, Dimensionality reduction of non-buoyant microconfined high-pressure transcritical fluid turbulence, Int. J. Heat Fluid Flow **102**, 109169 (2023).
[37] D. Y. Peng and D. B. Robinson, A new two-constant equation of state, Ind. Eng. Chem. Fund. **15**, 59 (1976).
[38] A. Firoozabadi, *Thermodynamics and Applications in Hydrocarbon Energy Production*, 1st ed. (McGraw-Hill Education, New York, NY, 2016).
[39] W. C. Reynolds and P. Colonna, *Thermodynamics: Fundamentals and Engineering Applications*, 1st ed. (Cambridge University Press, Cambridge, UK, 2019).
[40] A. Burcat and B. Ruscic, Third millennium ideal gas and condensed phase thermochemical database for combustion with updates from active thermochemical tables, Technical Report (Argonne National Laboratory, Lemont, IL, 2005).
[41] J. R. Elliott and C. T. Lira, *Introductory Chemical Engineering Thermodynamics* (Prentice Hall, Upper Saddle River, NJ, 2012).
[42] T. H. Chung, L. L. Lee, and K. E. Starling, Applications of kinetic gas theories and multiparameter correlation for prediction of dilute gas viscosity and thermal conductivity, Ind. Eng. Chem. Fund. **23**, 8 (1984).
[43] T. H. Chung, M. Ajlan, L. L. Lee, and K. E. Starling, Generalized multiparameter correlation for nonpolar and polar fluid transport properties, Ind. Eng. Chem. Res. **27**, 671 (1988).
[44] T. Watanabe, K. Tanaka, and K. Nagata, Solenoidal linear forcing for compressible, statistically steady, homogeneous isotropic turbulence with reduced turbulent Mach number oscillation, Phys. Fluids **33**, 095108 (2021).
[45] D. Martín and L. Jofre, High-fidelity database of supercritical homogeneous isotropic turbulence in the pseudo-boiling region, Sci. Data **12**, 1391 (2025).
[46] L. Jofre, A. Abdellatif, and G. Oyarzun, RHEA—An open-source reproducible hybrid-architecture flow solver engineered for academia, J. Open Source Softw. **8**, 4637 (2023).
[47] A. Abdellatif, J. Grau, R. Torres, and L. Jofre, OpenACC acceleration of parallel direct numerical simulation of turbulent flows, J. Appl. Comput. Mech. **11**, 425 (2025).
[48] S. Gottlieb, C. W. Shu, and E. Tadmor, Strong stability-preserving high-order time discretization methods, SIAM Rev. **43**, 89 (2001).
[49] G. Coppola, F. Capuano, S. Pirozzoli, and L. de Luca, Numerically stable formulations of convective terms for turbulent compressible flows, J. Comput. Phys. **382**, 86 (2019).

[50] G. Coppola, F. Capuano, and L. de Luca, Discrete energy-conservation properties in the numerical simulation of the Navier-Stokes equations, Appl. Mech. Rev. **71**, 010803 (2019).

[51] M. Bernades, F. Capuano, F. X. Trias, and L. Jofre, Energy-preserving stable computations of high-pressure supercritical fluids turbulence, *Proceedings of the 8th European Congress on Computational Methods in Applied Sciences and Engineering* (ECCOMAS, Oslo, Norway, 2022), pp. 1–12.

[52] M. Bernades, L. Jofre, and F. Capuano, Investigation of a novel numerical scheme for high-pressure supercritical fluids turbulence, *Proceedings of the Summer Program 2022, Center for Turbulence Research, Stanford University* (2022), p. 225.

[53] M. Bernades, L. Jofre, and F. Capuano, Kinetic-energy- and pressure-equilibrium-preserving schemes for real-gas turbulence in the transcritical regime, J. Comput. Phys. **493**, 112477 (2023).

[54] J. Janin, F. Duval, C. Friess, and P. Sagaut, A new linear forcing method for isotropic turbulence with controlled integral length scale, Phys. Fluids **33**, 045127 (2021).

[55] L. Jofre and J. Urzay, A characteristic length scale for density gradients in supercritical monocomponent flows near pseudoboiling, Annual Research Briefs, Center for Turbulence Research, Stanford University (2020), p. 277, https://web.stanford.edu/group/ctr/ResBriefs/2020/27_Jofre.pdf.

[56] E. Hurtán, C. Monteiro, M. Jofre, J. Casals-Terré, and L. Jofre, Data-informed characterization of spatio-temporal scales in experiments of microconfined high-pressure transcritical turbulence, Exp. Therm. Fluid Sci. **159**, 111282 (2024).

[57] C. Monteiro and L. Jofre, Resolution standards for direct numerical simulation of wall turbulence in high-pressure transcritical fluids, Phys. Fluids **36**, 125184 (2024).

[58] T. Passot and A. Pouquet, Numerical simulation of compressible homogeneous flows in the turbulent regime, J. Fluid Mech. **181**, 441 (1987).

[59] P. E. Lapenna, Characterization of pseudo-boiling in a transcritical nitrogen jet, Phys. Fluids **30**, 077106 (2018).

[60] S. Kawai, H. Terashima, and H. Negishi, A robust and accurate numerical method for transcritical turbulent flows at supercritical pressure with an arbitrary equation of state, J. Comput. Phys. **300**, 116 (2015).

[61] J. Jiménez, A. A. Wray, P. G. Saffman, and R. S. Rogallo, The structure of intense vorticity in isotropic turbulence, J. Fluid Mech. **255**, 65 (1993).

[62] S. B. Pope, *Turbulent Flows* (Cambridge University Press, Cambridge, UK, 2000).

[63] J. C. Wyngaard, The effect of velocity sensitivity on temperature derivative statistics in isotropic turbulence, J. Fluid Mech. **48**, 763 (1971).

[64] H. Pitsch and H. Steiner, Scalar mixing and dissipation rate in large-Eddy simulations of non-premixed turbulent combustion, Proc. Combust. Inst. **28**, 41 (2000).

[65] D. Martín, J. Grau, and L. Jofre, Conditional POD for predicting extreme events in turbulent flow time signals, Sci. Rep. **15**, 29629 (2025).

[66] L. Brandt and F. Coletti, Particle-laden turbulence: Progress and perspectives, Annu. Rev. Fluid Mech. **54**, 159 (2022).

[67] P. K. Yeung, D. A. Donzis, and K. R. Sreenivasan, Dissipation, enstrophy and pressure statistics in turbulence simulations at high Reynolds numbers, J. Fluid Mech. **700**, 5 (2012).

[68] H. Pitsch, Large-Eddy simulation of turbulent combustion, Annu. Rev. Fluid Mech. **38**, 453 (2006).

[69] A. N. Kolmogorov, A refinement of previous hypotheses concerning the local structure of turbulence in a viscous incompressible fluid at high Reynolds number, J. Fluid Mech. **13**, 82 (1962).

[70] M. S. Dodd and L. Jofre, Small-scale flow topologies in decaying isotropic turbulence laden with finite-size droplets, Phys. Rev. Fluids **4**, 064303 (2019).

[71] L. Warwaruk and S. Ghaemi, Local flow topology of a polymer-laden turbulent boundary layer, J. Fluid Mech. **983**, A22 (2024).

[72] E. A. Guggenheim, The principle of corresponding states, J. Chem. Phys. **13**, 253 (1945).

[73] K. S. Pitzer, D. Z. Lippmann, R. F. Curl, C. M. Huggins, and D. E. Petersen, The volumetric and thermodynamic properties of fluids. II. Compressibility factor, vapor pressure and entropy of vaporization, J. Am. Chem. Soc. **77**, 3433 (1955).

[74] D. Martín and L. Jofre, Supercritical homogeneous isotropic turbulence in the pseudo-boiling region database, Figshare+, Dataset (2025), https://doi.org/10.25452/figshare.plus.28751696.v1.

[75] P. C. Ma, X. I. A. Yang, and M. Ihme, Structure of wall-bounded flows at transcritical conditions, Phys. Rev. Fluids **3**, 034609 (2018).

[76] K. Kim, J. P. Hickey, and C. Scalo, Pseudophase change effects in turbulent channel flow under transcritical temperature conditions, J. Fluid Mech. **871**, 52 (2019).

[77] J. P. Hickey, P. C. Ma, M. Ihme, and S. S. Thakur, Large eddy simulation of shear coaxial rocket injector: Real fluid effects, *Proceedings of the 49th AIAA/ASME/SAE/ASEE Joint Propulsion Conference* (AIAA, Reston, VA, 2013).

[78] A. Congiunti and C. Bruno, Supercritical combustion properties, *Proceedings of the 41st Aerospace Sciences Meeting and Exhibit* (American Institute of Aeronautics and Astronautics, Reston, VA, 2003).

[79] P. Linstrom, NIST Chemistry Webbook, NIST standard reference database 69 (1997).

[80] P. K. Yeung, K. R. Sreenivasan, and S. B. Pope, Effects of finite spatial and temporal resolution in direct numerical simulations of incompressible isotropic turbulence, Phys. Rev. Fluids **3**, 064603 (2018).

[81] Xiang I. A. Yang, J. Hong, M. Lee, and Xinyi L. D. Huang, Grid resolution requirement for resolving rare and high intensity wall-shear stress events in direct numerical simulations, Phys. Rev. Fluids **6**, 054603 (2021).

[82] G. Barea, N. Masclans, and L. Jofre, Multiscale flow topologies in microconfined high-pressure transcritical fluid turbulence, Phys. Rev. Fluids **8**, 054608 (2023).

[83] D. A. Donzis, P. K. Yeung, and K. R. Sreenivasan, Dissipation and enstrophy in isotropic turbulence: Resolution effects and scaling in direct numerical simulations, Phys. Fluids **20**, 045108 (2008).